Instantaneous characteristics of interacting opposing plane jets in a generic enclosure measured with PIV

Experiments in Fluids (2023) 64:19
https://doi.org/10.1007/s00348-022-03549-9

RESEARCH ARTICLE

Instantaneous characteristics of interacting opposing plane jets in a generic enclosure measured with PIV

J-H. Thysen[1] · T. van Hooff[2] · B. Blocken[1,2] · G. J. F. van Heijst[3]

Received: 5 May 2022 / Revised: 6 December 2022 / Accepted: 6 December 2022

Abstract

Knowledge of the instantaneous flow behaviour of interacting opposing jets, in addition to knowledge of the mean flow, is important for science and practice. Whereas studies often focused on axisymmetric jets, analyses for plane jets are scarce in general and for plane jets in an enclosed domain (i.e. not a (semi-)open environment) in particular, as e.g. encountered in airplane cabin ventilation. In this paper, 2D particle image velocimetry measurements are performed to study isothermal interacting opposing plane wall jets and plane free jets in a generic empty reduced-scale water-filled enclosure. Inlet Reynolds numbers vary from 3450 to 4650. The analyses encompass an inspection of the global flow patterns (in the vertical midplane) and of the flow components (e.g. interaction zone, merged jet, return flows, recirculation cells), using distribution plots, correlation functions and fast Fourier transforms. Vortical structures are also visualised and tracked over time. It is shown that the transient interaction of the opposing wall jets drives a merged jet that resembles a flapping turbulent plane jet. Remarkable are the occasional deviating (more unstable) flow patterns that appear. Furthermore, many vortical structures are present that could enhance mixing within the enclosure. The opposing free jets mainly show quasi-periodic oscillations with a given frequency (Strouhal number around 3.3×10^{-3}), comparable to opposing plane free jets mentioned in the literature. Also in this configuration, many different vortices are present that can grow considerably large while transported through the flow domain. Both configurations show a potential for contaminant lock-up (stagnation zones).

✉ J-H. Thysen
johendrik.thysen@kuleuven.be

[1] Building Physics and Sustainable Design, Department of Civil Engineering, KU Leuven, Kasteelpark Arenberg 40 – bus 2447, 3001 Leuven, Belgium

[2] Building Physics and Services, Department of the Built Environment, Eindhoven University of Technology, P.O. Box 513, 5600 MB Eindhoven, The Netherlands

[3] Fluids and Flows, Department of Applied Physics, Eindhoven University of Technology, P.O. Box 513, 5600 MB Eindhoven, The Netherlands

Published online: 07 January 2023

Graphical abstract

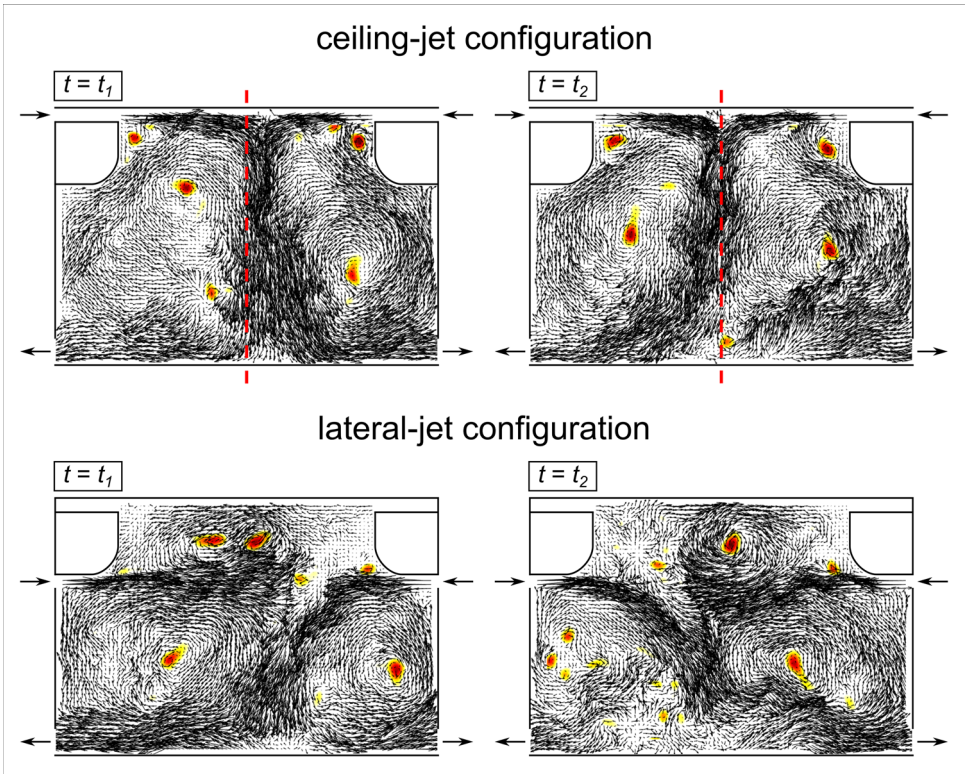

1 Introduction

Counterflowing jets emerging from opposing inlet slots that impinge on each other, i.e. so-called opposing jets, appear in numerous engineering applications: confined impinging-jets reactors (e.g. Liu and Fox 2006), side-dump combustors (e.g. Samaniego et al. 1993), vertical and/or short take-off and landing (V/STOL) aircrafts (e.g. Kotansky and Glaze 1980), air distribution system in an airplane cabin (e.g. Cao et al. 2014), etc. The impingement point of the opposing jets (hereafter referred to as the interaction zone) is highly turbulent and may be hydrodynamically unstable, depending on many parameters, such as the inlet Reynolds numbers (Re_0), the jet-separation distance (d), the level of confinement and the inlet slot height (h) and shape, as observed from different theoretical, experimental and numerical studies (e.g. Denshchikov et al. 1978, 1983; Rolon et al. 1991; Wood et al. 1991; Champion and Libby 1993; Zhao and Brodkey 1998; Besbes et al. 2003; Pawlowski et al. 2006; Zhao et al. 2008; Liu et al. 2010; Li et al. 2011, 2013; Tu et al. 2014; Hassaballa and Ziada 2015; Ansari 2018).

Although the majority of studies considered axisymmetric jets (Li et al. 2013), of interest in the present study are opposing plane (2D) jets. For example, Denshchikov et al. (1978, 1983) performed experiments on the interaction of opposing plane water jets submerged in a relatively large water tank. Depending on two bifurcation parameters, i.e. Re_0 ($100 < Re_0 < 4800$) and the aspect ratio (AR) determined from d and h ($AR = d/h > 4$–6), observations were made in which one jet overlaps the other alternately with a frequency determined by the two parameters (i.e. so-called deflecting oscillations). 2D numerical results by Pawlowski et al. (2006) reported different flow regimes for symmetric laminar opposing plane jets, controlled by the same two bifurcation parameters ($1 < Re_0 < 1500$; $1 < AR < 20$). Multiple stable and unstable steady states were observed, as well as the periodic deflecting oscillation (similar to Denshchikov et al. 1978, 1983) and a chaotic flow regime. Also Li et al. (2011) detected different flow regimes in their experimental work on unconfined plane opposing air jets (for $786 < Re_0 < 6288$; $1 < AR < 20$), which were characterised by either an irregular oscillation of the interaction zone along the jets centreline or the periodic deflecting oscillation with a specific oscillation frequency. This frequency was observed to decrease for larger jet-separation distances or lower inlet Reynolds numbers. Additional results to the study of Li et al. (2011)

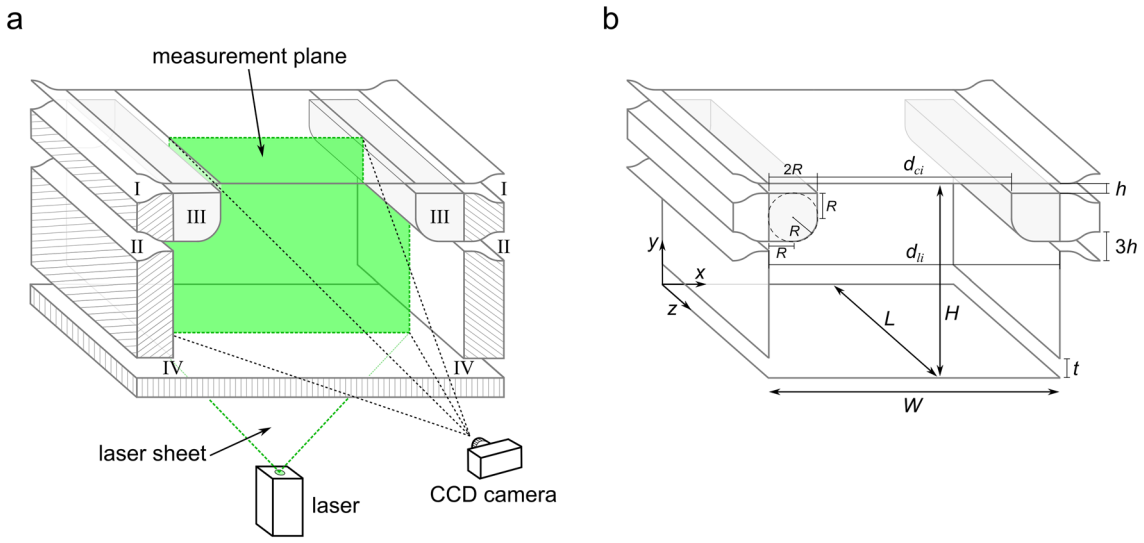

Fig. 1 **a** Experimental set-up with PIV equipment (laser and CCD camera), laser sheet illuminating vertical measurement plane (in green), ceiling inlets (I), lateral inlets (II), OHSCs (III) and outlets (IV); **b** indication of dimensions of enclosure (height *H*, width *W*, length *L*), inlet height (*h*), outlet height (*t*), radius of OHSCs (*R*) and separation distance between ceiling (d_{ci}) and lateral (d_{li}) inlet slots

were provided by Tu et al. (2014) (for $16 < Re_0 < 5000$; $2 < AR < 40$), who experimentally and numerically showed that the deflecting oscillation frequency also lowered (or even disappeared) when the plane jets were subjected to confinement boundaries or for increased width-to-height inlet slot ratios. Similar sensitivities to the jet-separation distance and inlet Reynolds number were reported by Hassaballa and Ziada (2015). They conducted particle image velocimetry (PIV) measurements of high-velocity impinging plane air jets (for $18{,}000 < Re_0 < 30{,}000$; $7 < AR < 130$) and linked the self-sustained deflecting oscillation to the high pressure in the interaction zone and the flow dynamics (circulation cells) in the entrainment regions of the jets.

Whereas the aforementioned studies focused on opposing plane free jets, interacting opposing plane wall jets were also investigated by e.g. Kind and Suthanthiran (1973), Gilbert (1985) and Johansson and Andersson (2005) in an open environment (i.e. not enclosed) or by Shishkina and Wagner (2012), Körner et al. (2013, 2015) and Kandzia and Mueller (2016, 2018) in a generic enclosure (model room for studying e.g. ventilation flows in airplane cabins) incorporating thermal buoyancy forces (mixed convection flow). Although in most of these experimental or numerical studies the flow was observed to be highly transient (and under mixed convection, in some cases, even unstable), mainly time-averaged flow characteristics were presented and an analysis of the instantaneous flow patterns, in particular of the transient jet interaction, was absent. Under mixed convection, a distinction between stable and unstable flow regimes was made, yet an actual transient characterisation of these (un)stable flow regimes was not incorporated. Such knowledge is essential for the effective use of opposing plane jets in applications that rely on their (un)stable behaviour (Pawlowski et al. 2006). Out of the aforementioned works on opposing plane wall jets, only Körner et al. (2013) (for $67 < Re_0 < 464$; AR ≈ 200) reported in more detail that the isothermal opposing jets in their generic enclosure induced (horizontal) oscillations of the large-scale flow structures at specific frequencies proportional to Re_0.

In the current paper, both opposing plane wall jets and opposing free jets in a reduced-scale water-filled generic enclosure are investigated (Fig. 1), hereafter called the ceiling-jet and lateral-jet configuration, respectively. The ceiling jets are located at the top of the enclosure (I in Fig. 1a), whereas the lateral jets (II), which are partially guided into the enclosure along a surface (III) (simplified representation of overhead stowage compartments—OHSCs—in a cabin), are located at a fixed distance from the ceiling. This set-up is, for example, a generic representation of (airplane) cabin mixing ventilation where opposing plane jets are used to provide fresh air to the cabin (Thysen et al. 2022a).

Previous studies on opposing-jet mixing ventilation in airplane cabins mainly focused on the time-averaged airflow field, whereas information on instantaneous flow patterns and their dynamics is also very important regarding, for example, the transmission of contaminants throughout the cabin or thermal comfort of the passengers, especially since the complex cabin airflow patterns can be very transient and unstable (e.g. Lin et al. 2005; Kühn et al. 2009). A few studies did elaborate on the instantaneous airflow dynamics using computational fluid dynamics (CFD) simulations (e.g. Yang et al. 2016; Wang et al. 2022) or PIV measurements

(e.g. Li et al. 2016, 2017; Wang et al. 2017). These studies pointed out quasi-periodic deflecting oscillations of the lateral jets (so-called large-scale swing motions), the oscillation frequency of which is affected by Re_0, the supply (direction) angle or the thermal load (Wang et al. 2022). In addition, the measurements provided a detailed flow analysis of specific areas, i.e. the jet interaction zone (Li et al. 2016; Wang et al. 2017) and/or the recirculation cells (Li et al. 2017). However, these studies all considered the same specific mock-up of a Boeing 737–200 single-aisle cabin and, given the complexity of the indoor cabin environment, the observed flow patterns may be case specific.

The objective of the current paper is to present 2D PIV measurements of the instantaneous isothermal flow driven by opposing jets in an empty generic cabin model (Fig. 1). Its reduced scale allows capturing the velocity field in the whole vertical cross-section with a high spatial resolution. The enclosure is generic and objects or heat sources (seats, passengers, etc.), typically present in airplane cabin mock-ups, are not included. This allows for a fundamental investigation of the dynamics of the flow components that are inherent to enclosed opposing-jet flows, such as the jet interaction and the merged jet developed after the interaction. The resulting large recirculation cells with return flows along the walls as well as the development and transport of vortical structures throughout the flow domain are also investigated. Furthermore, a comparison with the results from the aforementioned studies on wall and free jets is provided. In addition, the experimental data will be useful for the validation of numerical simulations and may be valuable to other applications involving opposing jets.

The structure of the paper is as follows. First, the experimental set-up and PIV settings are described in Sect. 2. Section 3 outlines the methods used for the analyses. In Sects. 4 and 5, the results for the ceiling-jet and lateral-jet configurations are presented, respectively. The limitations of the current study and future work are described in Sect. 6, and Sect. 7 provides the conclusions.

2 Experimental set-up and PIV settings

The experimental set-up is more extensively described in a previous paper by the authors (Thysen et al. 2022a) and only a brief outline is thus provided here. The set-up is shown in Fig. 1 and consists of a water-filled enclosure equipped with two pair of full-length inlets at opposing sides: ceiling inlets at the top (I) and lateral inlets (II) located below the OHSCs (III). Upstream of each inlet, a conditioning section is incorporated with three screens (having a decreasing porosity downstream), a honeycomb (not shown in Fig. 1) and a contraction to minimise the turbulence levels and velocity gradients in the supply flows (for details see Thysen et al. 2022a). Every inlet is connected to a water storage tank via a STAD DN 40 valve, which enables regulation of the flow rate of the particular inlet. A centrifugal pump (Wilo-VeroLine-IP-E50) drives the flow. Water leaves the enclosure through the two full-length outlets at floor level (IV), after which it flows back to the water storage tank (closed system). Isothermal conditions are applied.

The enclosure is at reduced scale (1:11) with height $H = 0.2$ m (Fig. 1b). The width W and length L both measure $1.5H$. The inlet height $h = 0.05H$ (before the contraction it is $3h$) and the height of the outlets $t = 0.1H$ (or $t = 2h$). The accuracy of h is 0.01 mm. Furthermore, the distance between the opposing inlets is $d_{ci} = H$ (or AR = 20) for the ceiling inlets, and $d_{li} = W = 1.5H$ (or AR = 30) for the lateral inlets. The OHSCs, which are a generic representation of those in an actual (airplane, train or bus) cabin, are comprised of a cuboid with a rounded part based on a circle with radius $R = 0.125H$. Note that the aim is to derive fundamental insights into the underlying flow components of the opposing-jet (ventilation) flow, which in reality is subjected to many cabin-specific parameters. Therefore, a generic set-up, being a simplified model—but still representative of an actual cabin—is employed.

2D PIV is applied to measure the flow in the vertical mid-plane of the enclosure ($z/H = 0.75$; Fig. 1a), using a Nd:YAG solid-state laser (double pulse, 2 × 160 mJ, 532 nm) with the laser sheet coming from below the set-up. The light is reflected by polyamide seeding particles (diameter 5–35 µm, density 1.03 g/cm^3) towards the charge-coupled device (CCD) camera (1200 × 1600 px) used for image recording. The PIV measurements are performed conforming to guidelines from the literature (e.g. Keane and Adrian 1990; Prasad 2000; Raffel et al. 2018) to minimise systematic errors, as already reported in detail in Thysen et al. (2022a). After regulation of the intended supply flow rate, a sufficient amount of time is taken into account to first allow the flow to adapt to the inlet conditions, which avoids measuring start-up effects. Then the flow is recorded for 15 min with a sampling frequency f_s of 15 Hz corresponding to $N = 13{,}500$ samples (image pairs). Each sample is analysed with the multi-grid interrogation method in which the interrogation windows reduce in size from 64 × 64 to 16 × 16 px (with 50% overlap) in three iterations (creating 195 × 130 measurement points P according to a spatial resolution of ≈ 1.54 mm). Spurious velocity vectors are limited to a minimum by only accepting vectors for which the peak-to-peak ratio is larger than 1.3 and the normalised median test lower than 3.0.

The ceiling-jet and lateral-jet configurations, as depicted in Fig. 2, are studied in this paper. Three different inlet Reynolds numbers of the supply jets are used per configuration: $Re_0 \approx 3450$, 4350 and 4650 (ceiling inlets) and $Re_0 \approx 3500$, 4300 and 4600 (lateral inlets), where $Re_0 = U_0 h/\nu$ with ν the kinematic viscosity of water at 20 °C and U_0 representing

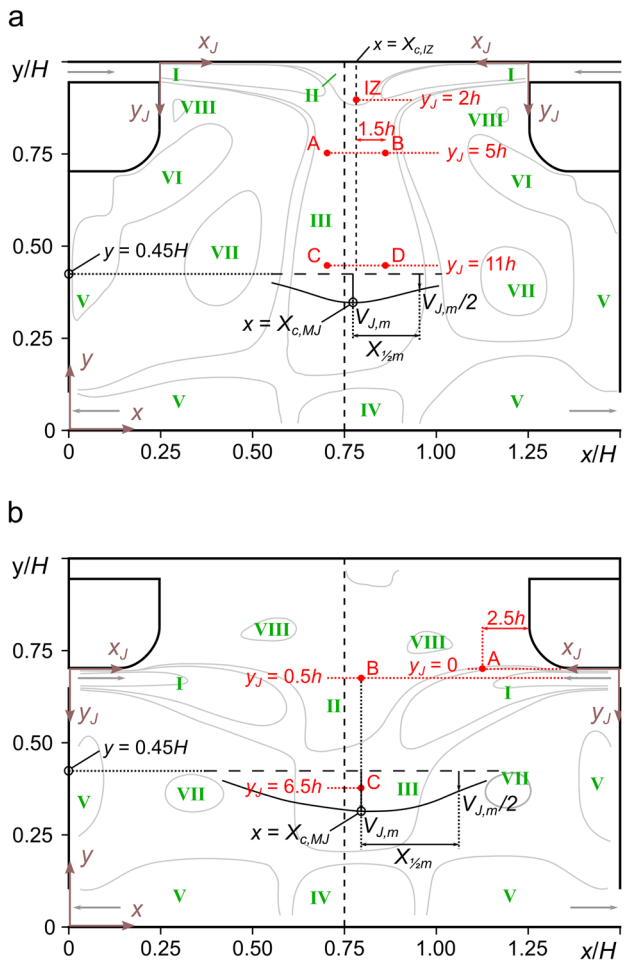

Fig. 2 Vertical cross-section of ceiling-jet configuration (**a**) and lateral-jet configuration (**b**), with visualisation of flow components using *mean* 2D velocity magnitude contours (for $Re_0 \approx 3450$ in **a**, $Re_0 \approx 3500$ in **b**): (I) ceiling/lateral jets, (II) interaction zone, (III) merged jet, (IV) impingement zone, (V) return flows along floor and sidewalls, (VI) return flows after detachment from OHSCs (only in **a**), (VII) large recirculation cells, (VIII) small recirculation cells. Also indicated are mean centre location of interaction zone $x=X_{c,IZ}$ (only in **a**), and merged-jet *mean* velocity profile at $y/H=0.45$ with mean centre location $x=X_{c,MJ}$, maximum mean velocity $V_{J,m}$ and half-velocity width $X_{½m}$. Red dots are locations of monitoring points

the average of the maximum mean (i.e. time-averaged) jet (x-)velocities $U_{J,0}$ at the two (ceiling/lateral) inlets. The values of $U_{J,0}$ differ by 1.5–5% (ceiling inlets) or 6–10% (lateral inlets). The procedure for matching both inlet velocities consists of an iterative process in which first the valves are set according to the desired flow rate (with an uncertainty on the flow rate around 5–7% for the selected valve openings). Then preliminary PIV measurements are performed and analysed to check on the agreement between the supply flow rates of the opposing inlets, after which the valve openings are readjusted if needed. The inlet turbulence intensities I_0 measure 4.5–6% (ceiling inlets) and 5.5–6% (lateral inlets), with I_0 representing the average of $I_{J,0}$ which differ around one to six percentage points (ceiling inlets) and less than one percentage point (lateral inlets). The relative statistical uncertainty on the measured mean velocity components is assessed to be below 13% ($Re_0 \approx 3450$), 6% ($Re_0 \approx 4350$) and 5% ($Re_0 \approx 4650$) in the configuration with ceiling inlets and lower than 5% ($Re_0 \approx 3500$), 4% ($Re_0 \approx 4300$) and 6% ($Re_0 \approx 4600$) in the configuration with lateral inlets (Thysen 2022).

The chosen Re_0 are based on those typically used for airplane cabin mixing ventilation (ASHRAE 2019), which produce transitional jets (Thysen et al. 2022a). The corresponding supply flow rates vary in the range of 1.03×10^{-3} to 1.40×10^{-3} m^3/s, resulting in water exchange rates of 224 to 303 h^{-1}. Following the calculations presented by Thatcher et al. (2004), using the length scale ratio of 1:11, and by taking into account Reynolds number matching (with the ratio of the kinematic viscosities of air to water equal to 15.03), the flow rate in a corresponding full-scale (air-filled) replica of the cabin model would be 165 times this of the current reduced-scale water-filled set-up. The air flow rate would then be in the range of 0.17–0.23 m^3/s, leading to an air exchange rate of 28–38 h^{-1}, which is in close agreement with this used in realistic airplane cabins (Hunt and Space 1994).

3 Methods

The instantaneous flow variables will be indicated by lower-case letters, while upper-case letters will be used for the mean variables. For example, u and v represent the instantaneous x- and y-velocity, respectively, with mean values U and V. Variables are either defined with respect to the coordinate system of the enclosure (x,y) located at the lower left corner of the vertical midplane (Fig. 2), or with respect to the coordinate system (x_J,y_J) located at the top of every inlet. In the latter case, the variables will be indicated with subscript 'J'.

3.1 Periodicity detection

In order to detect whether the flow shows specific periodicities (such as the deflecting oscillation mentioned in Sect. 1), time series of u and v obtained in different monitoring points, some of which are shown in Fig. 2, are analysed using two approaches:

The (normalised) correlation function between two time series $a(t)$ and $b(t)$ is defined as

$$C_{ab}(\tau) = \frac{\sum_{i=1}^{N} a'(t_i) b'(t_i+\tau)}{\sqrt{\sum_{i=1}^{N} a'(t_i)^2}\sqrt{\sum_{i=1}^{N} b'(t_i)^2}} \quad (1)$$

where the apostrophe indicates the fluctuation of the corresponding variable (e.g. $a' = a - A$), N is the number of PIV samples and τ represents the time separation between the two series. In the case $a(t) = b(t)$, C_{ab} is called the autocorrelation function (ACF), otherwise it is referred to as the cross-correlation function (CCF). The correlation coefficient, defined as $C_{ab}(\tau = 0)$, measures the linear dependence between the two time series. In the case the time series contain periodicity, C_{ab} shows peaks at each multiple of the given period.

The (1D) energy spectrum of the velocity fluctuations $u'(t)$ or $v'(t)$, denoted as $E_{u'u'}$ or $E_{v'v'}$, respectively, which shows the amount of kinetic energy as a function of frequency, is calculated following Welch's method (e.g. Stoica and Moses 2005). It encompasses a subdivision of the time series into eight segments of equal length with 50% overlap (each containing 3000 samples, corresponding to an interval length of 200 s), which are windowed (Hamming window) and used for FFT. The resulting individual energy spectra are then averaged to obtain the final energy spectrum of the time series. This provides a spectrum with reduced noise, but at the expense of a reduced frequency resolution (i.e. 5×10^{-3} Hz instead of 1.11×10^{-3} Hz). Dominant frequencies (periods) present in the time series will have a peak in the energy spectrum.

As outlined in e.g. Vlachos et al. (2005) and Puech et al. (2020), using both methods is beneficial since on the one hand the energy spectrum can be contaminated with spectral leakage and deteriorates in accuracy for large periods. On the other hand, the correlation function can provide better accuracy (also for longer periods), but can be more difficult to interpret (e.g. multiplicity of peaks per period).

3.2 Vortex identification

Vortices are visualised by means of velocity vectors, from which the area-averaged (background) velocity may be subtracted for better visibility, and using the vortex centre identification algorithm outlined in Graftieaux et al. (2001) and Zigunov (2021), in which the dimensionless scalar function Γ is evaluated at every measurement point P in the vertical midplane according to:

$$\Gamma(P) = \frac{1}{n} \sum_{Q \in S} \frac{\left(\vec{r}_{PQ} \times \vec{u}_Q \right) \cdot \hat{k}}{\left| \vec{r}_{PQ} \right| \left| \vec{u}_Q \right|} = \frac{1}{n} \sum_{Q \in S} \sin\left(\alpha_Q \right) \tag{2}$$

This function considers a (circular) interrogation window S with fixed size centred around P containing n other measurement points Q. It calculates the cross-product between the radius vector ($\vec{r}_{PQ}$), defined from P to Q, and the velocity vector at point Q ($\vec{u}_Q$), which, after application of the dot product with the unit vector normal to the measurement plane ($\hat{k}$), is divided by the magnitude $|.|$ of each vector; this is equivalent to the sine of the angle between both vectors (α_Q). Summation over all points Q and division by n yields $\Gamma(P)$. Note that Γ shows equivalence with the angular momentum of a solid body rotation (Graftieaux et al. 2001).

The size of S (or n) controls the size of the vortices to be detected and therefore acts as a spatial filter (small-scale vortices are not visualised when n becomes too large). Within the vortex centre, $|\Gamma|$ is maximum and bounded by 1. Note that its maximum value decreases when vortices deviate from an axisymmetric shape and that therefore its range (i.e. value at the lower end) will be adjusted accordingly for best visualisation of the vortices.

It should be mentioned that other vortex identification methods were tested, such as the vorticity or Okubo–Weiss function; however, these resulted in very noisy images from which no clear vortical structures could be distinguished.

4 PIV measurement results: ceiling inlets

4.1 Mean flow

An impression of the mean flow field in the vertical midplane for each Re_0 of the ceiling jets is shown in Fig. 3. Note that only one out of three velocity vectors is shown for the sake of clarity. Since a thorough discussion on the mean flow field was presented in a previous paper by the authors (Thysen et al. 2022a), only the main characteristics relevant to the current paper are recapitulated here. The mean flow field was obtained after averaging all PIV samples (15 min) which, according to convergence plots, was assessed to be sufficiently long (see Thysen et al. 2022a). The two plane jets emerging from the ceiling inlets (I in Fig. 2a) interact nearby the middle of the ceiling ($x/H = 0.75$) and try to displace each other, thereby inducing an adverse pressure gradient which leads to separation of both jets from the ceiling. In all cases, the created interaction zone (separation bubble; II in Fig. 2a) is located slightly to the right of the vertical centreline (i.e. $X_{c,IZ}/H > 0.75$, with $X_{c,IZ}$ denoting its mean centre location,[1] indicated in Fig. 2a), due to the left jet having slightly higher velocity than the right jet (Sect. 2). A downward flowing merged jet is present (III in Fig. 2a), flowing almost parallel to (Fig. 3a) or slightly curving away from (Fig. 3b,c) the vertical, as indicated by the green dash-dotted lines that visualise the mean centre location of the merged

[1] $X_{c,IZ}$: mean value of the (instantaneous) centre location of the interaction zone $x_{c,IZ}$, which is the location of minimum (zone-averaged) 2D velocity magnitude $|v| = (u^2 + v^2)^{1/2}$ within the area between the two ceiling inlets ($0.25 < x/H < 1.25$) and with height $y_J = 2h$ from the ceiling.

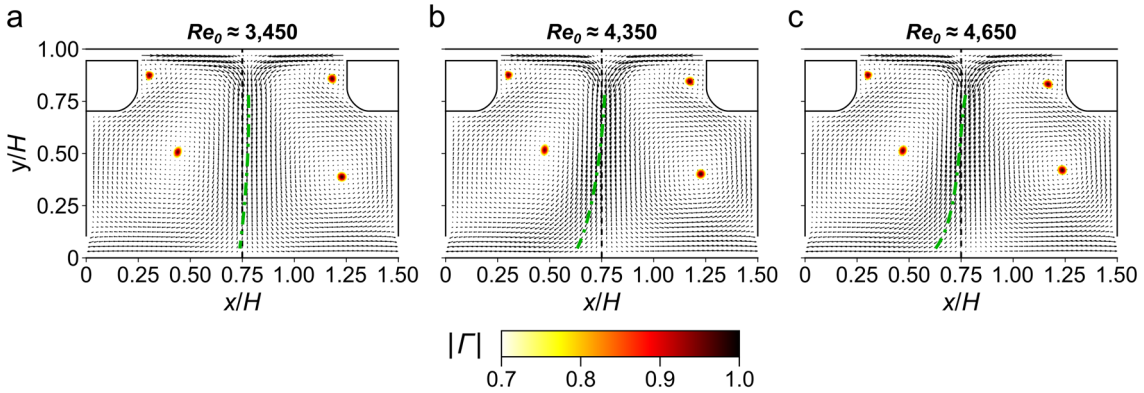

Fig. 3 Mean velocity vectors and contours of $|\Gamma|$ in vertical midplane of ceiling-jet configuration for three Re_0: **a** $Re_0 \approx 3450$, **b** $Re_0 \approx 4350$ and **c** $Re_0 \approx 4650$. Green dash-dotted lines indicate $X_{c,MJ}$ over full height of merged jet

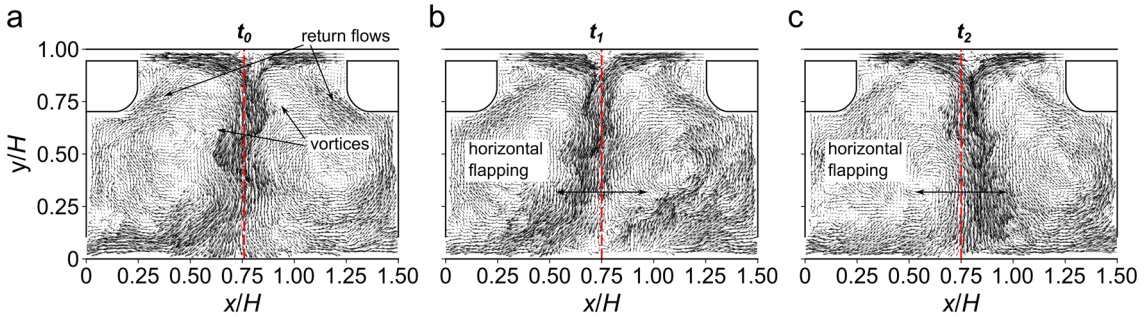

Fig. 4 Instantaneous velocity vectors in vertical midplane of ceiling-jet configuration for $Re_0 \approx 4350$ showing typical movement of interaction zone and merged jet, with indication of **a** vortices and **b**, **c** flapping movement. Red dashed line is vertical centreline of enclosure ($x/H = 0.75$). Corresponding animation is Online Resource 1

jet[2] $X_{c,MJ}$. Also, asymmetry between the two half-velocity widths $X_{½m}$ of the merged jet (right side has larger width) is observed from $y/H < 0.5$ (only slightly visible in Fig. 2a; see Thysen et al. 2022a for full description). The merged jet then impinges on the floor (IV in Fig. 2a), after which part of the flow is extracted from the enclosure via the outlets and part returns along the sidewalls and the OHSCs (V and VI). Two large (VII) and two smaller (VIII) recirculation cells are established, the centres of which are visualised in Fig. 3 using $|\Gamma|$ (Eq. 2).

4.2 Instantaneous flow: overall flow behaviour

Figure 4 shows for $Re_0 \approx 4350$ velocity vector fields of several characteristic (typical) instantaneous flow patterns, which are also observed for the other Re_0. An animation (Online Resource 1) is included in the supplementary information section. Note that only one out of two vectors is presented. The transient interaction of the opposing ceiling jets results in a horizontal movement of the interaction zone, which also causes the merged jet to alternate left and right. The distribution of the (instantaneous) merged jet location $x_{c,MJ}$, which is recorded at every instant and for each Re_0, is shown in Fig. 5a. The relative frequency indicates the number of PIV samples with $x_{c,MJ}/H$ located at $x/H \pm \delta x$ (with $\delta x = 0.0125H$), relative to the total number of samples. Note that the range of x/H is restricted to 0.25–1.25, which are the locations of the two ceiling inlet slots. For all three Re_0, the distributions have their maximum around the centreline of the enclosure ($x/H = 0.75$), indicating that most of the time the merged jet is located here. The distribution of $Re_0 \approx 3450$ is somewhat broader than for the other two Re_0 (the locations of the two bins at the left and right outer side of the distributions are indicated in the table in Fig. 5a), which demonstrates a larger range of locations over which the merged jet moves. The range of $x_{c,MJ}$ covers 50% of W for $Re_0 \approx 3450$, compared to 39% and 34% in $Re_0 \approx 4350$ and $Re_0 \approx 4650$, respectively. All distributions have

[2] $X_{c,MJ}$: mean value of the (instantaneous) centre location of the merged jet $x_{c,MJ}$, which is the location of maximum (zone-averaged) y-velocity in the merged jet ($v_{J,m}$) within the area covered by the full width and $0.3 < y/H < 0.6$ (or $8 < y_J/h < 14$).

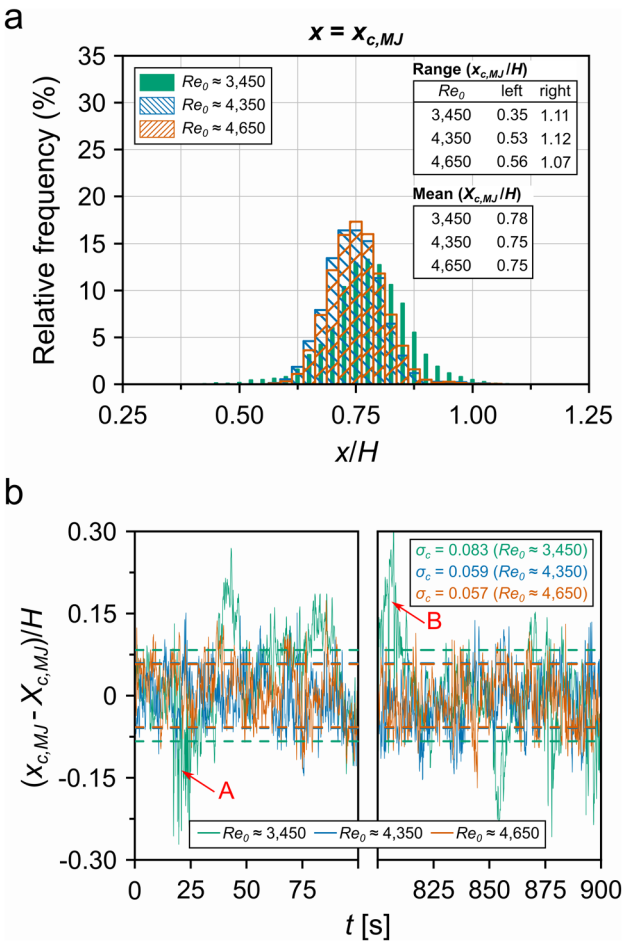

Fig. 5 Centre location of merged jet ($x_{c,MJ}$) in ceiling-jet configuration for three Re_0: **a** distribution plots and **b** fragments of corresponding time series. Tables in **a** indicate range of $x_{c,MJ}$ and its mean value ($X_{c,MJ}$). Time series of $x_{c,MJ}$ in **b** represent fluctuation from mean centre location ($x_{c,MJ}$–$X_{c,MJ}$), with standard deviations σ_c shown by dashed lines

mean locations $X_{c,MJ}$ slightly at the right of the centreline $x/H = 0.75$ (table in Fig. 5a).

The corresponding time series of $x_{c,MJ}/H$ are shown in Fig. 5b, represented with respect to $X_{c,MJ}$. Note that, for the sake of clarity, only two fragments (first and last 100 s) of the full time series are shown. The fluctuating movement around $X_{c,MJ}$ is clearly visible, with frequent stronger deviations at $Re_0 \approx 3450$, which are not present for the other two Re_0 (also note the higher standard deviation σ_c for this Re_0, indicated with dashed lines in Fig. 5b). At such instances, the merged jet is located at the outer edges of the distributions (Fig. 5a) for a longer period of time (≈ 20 to 60 s), e.g. at $60 < t < 90$ s, indicating that one ceiling jet suppresses the other opposing jet, after which the flow recovers back to the transient movement around $X_{c,MJ}$. Sometimes, the flow at $Re_0 \approx 3450$ can even deviate from the common flow patterns (Fig. 4), at e.g. instances indicated with letters A and B in Fig. 5b. Figure 6 shows several instantaneous velocity vector fields recorded around instance A, with the corresponding flow animation presented in Online Resource 2 (Online Resource 3 presents the animation of the flow around instance B). Note that only one out of two vectors is shown. At such instances, the merged jet can also move significantly away from the centreline. Ten such events are observed during the recording and appear to occur at random instances (i.e. with unequal time intervals in between). The reason for such persistent deviations from $X_{c,MJ}$ and the occurrence of deviant flow patterns for $Re_0 \approx 3450$ may be attributed to the more equal inlet velocities (momentum) of the interacting ceiling jets in this measurement (i.e. 1.5% difference in $U_{J,0}$ for $Re_0 \approx 3450$, compared to a difference of up to 5% for the two other Re_0); it may be argued that a stronger discrepancy between the jet momenta results in a more stable interaction zone due to one jet being suppressed more by the other jet, although an indisputable explanation is not obtained. Similar results as presented in Fig. 5 are obtained for the location of the interaction zone $x_{c,IZ}$—which are not shown here for the sake of brevity (the interested reader is referred to Thysen 2022 in this regard)—indicating that the merged jet follows the movement of the interaction zone, which is confirmed by the CCF (Eq. 1) of their time series, having a maximum value of 0.4 at $\tau < 0$ (not shown). As already mentioned by Johansson and Andersson (2005), the transient interaction zone acts as an "apparent unstable virtual source" of the merged jet.

The alternating movement of the merged jet resembles the flapping of a turbulent (impinging) plane jet (e.g. Cervantes de Gortari and Goldschmidt 1981; Khayrullina et al. 2017). To investigate this apparent jet flapping, time series of the velocity recorded in different monitoring points (see Fig. 2a), which are located symmetrically along both sides of the merged jet close to the point of its formation (points A and B) and further downstream (points C and D), are analysed. Figure 7a shows a fragment of the time series of v' (made dimensionless using U_0) for each pair of monitoring points in the measurement with $Re_0 \approx 3450$. The corresponding moving average (over 1 s recording time) is plotted on top of each time series (solid and dotted black lines) to accentuate the (larger-scale) fluctuations. The time series show quasi-periodic oscillations and, as the velocity at one point decreases, the velocity at the opposing point generally increases, which is also demonstrated in Fig. 7b by the negative value of the corresponding correlation coefficient ($C_{vv}(0) < 0$). Note that the range of C_{vv} is restricted for better visibility. The correlation is strongest at the onset of the merged jet (points A and B; $C_{vv}(0) = -0.68$) and decreases further downstream (points C and D; $C_{vv}(0) = -0.32$). The CCFs also alternate between positive and negative values, seemingly quasi-periodic. These observations ($C_{vv}(0) < 0$ and

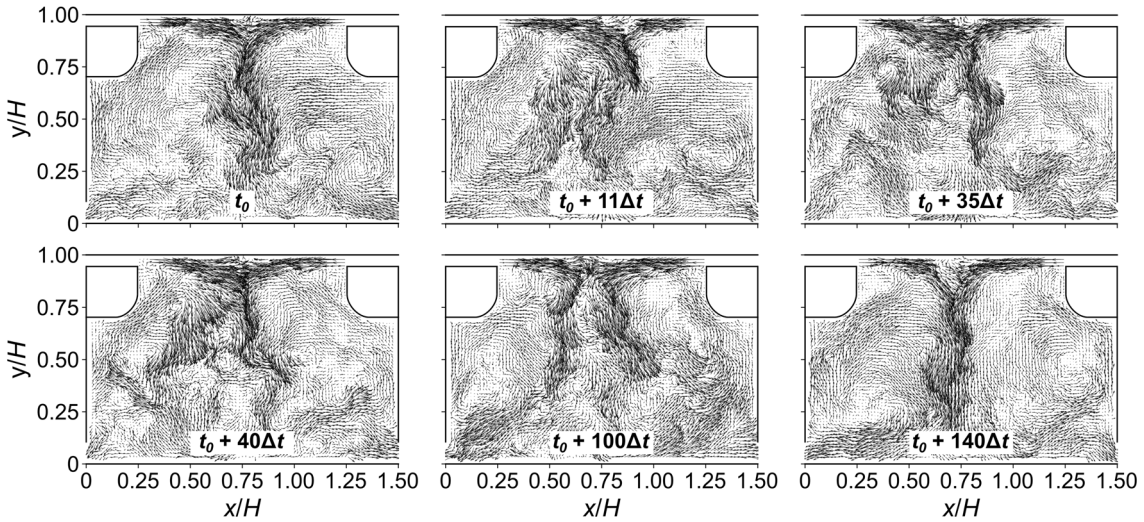

Fig. 6 Instantaneous velocity vectors in vertical midplane showing a particular occurrence of deviating flow patterns in ceiling-jet configuration for $Re_0 \approx 3450$ around instance A indicated in Fig. 5b. Note that images are not equally spaced in time and Δt is time step (equal to f_s^{-1}). Corresponding animation is Online Resource 2

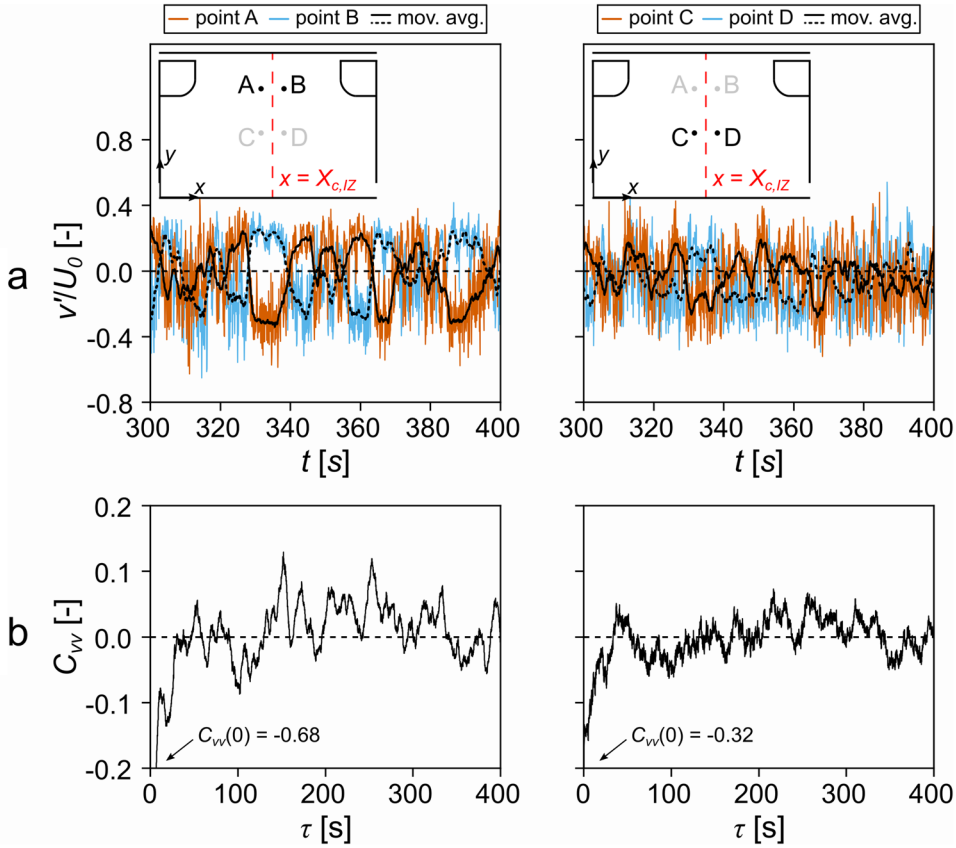

Fig. 7 Fragment (100 s) of time series of dimensionless y-velocity fluctuations (v'/U_0) in ceiling-jet configuration for $Re_0 \approx 3450$ (**a**), with corresponding CFF C_{vv} (**b**) in two pairs of monitoring points (see also Fig. 2a): points A and B (left), points C and D (right)

quasi-periodicity) are signs of a flapping merged jet, as opposed to a puffing-like motion, according to Cervantes de Gortari and Goldschmidt (1981). Similar observations hold for the other Re_0.

The quasi-periodicity is further investigated by application of FFT on the recorded time series. Figure 8 plots the resulting dimensionless 1D energy spectrum of v' ($E_{v'v'}/U_0^2$) as a function of the Strouhal number $St = fh/U_0$ (f being the

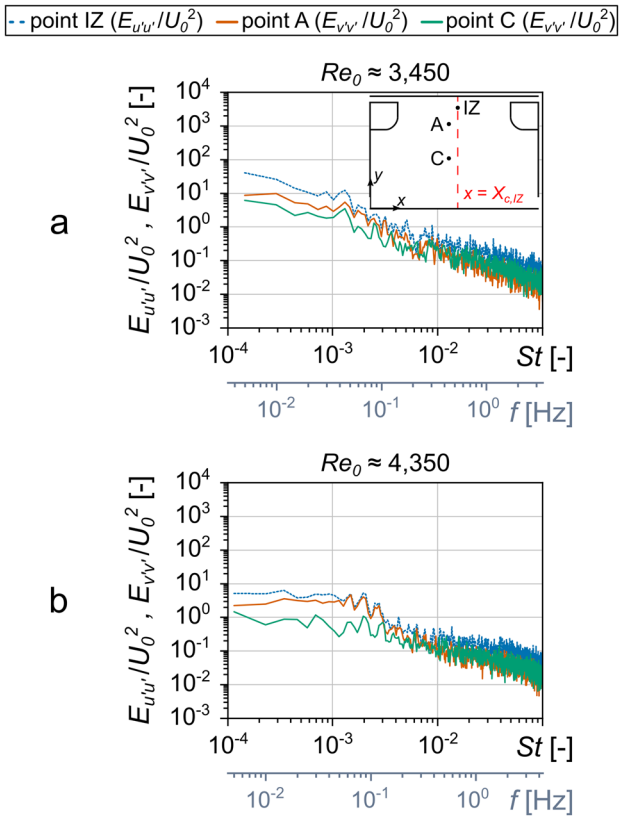

Fig. 8 Dimensionless 1D energy spectra of v' ($E_{v'v'}/U_0^2$) in monitoring points A and C (see also Fig. 2a) together with reference energy spectrum of u' ($E_{u'u}/U_0^2$) in monitoring point IZ, in ceiling-jet configuration for: **a** $Re_0 \approx 3450$, **b** $Re_0 \approx 4350$

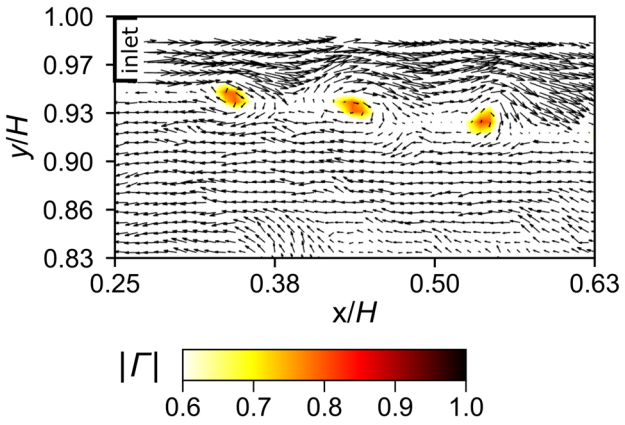

Fig. 9 Vortex train in outer layer of (left) ceiling jet ($Re_0 \approx 3450$) visualised by instantaneous velocity vectors from which area-averaged instantaneous velocity is subtracted, together with contours of $|\Gamma|$

frequency) obtained in monitoring points A and C for $Re_0 \approx 3450$ and $Re_0 \approx 4350$. The spectrum of u' in point IZ (see Fig. 2a) is also added as a reference (dashed line). Although the energy level appears to be (slightly) increased for $St < 1.7 \cdot 10^{-3}$ (or $f < 0.06$ Hz) for $Re_0 \approx 3450$, and $St < 2.8 \cdot 10^{-3}$ ($f < 0.11$ Hz) for $Re_0 \approx 4350$, a specific characteristic frequency is not observed. The results for $Re_0 \approx 4650$ (not shown) are similar to these of $Re_0 \approx 4350$.

In order to assess to which extent the merged jet movement is affected by the return flows that detach from the OHSC (Fig. 4a, $y/H = 0.7$), correlations (Eq. 1) between time series of several return flow characteristics (e.g. velocity magnitude $|v|$, angle with respect to the horizontal at which the return flows approach the merged jet θ_{RF}) and characteristics of the merged jet (e.g. $X_{c,MJ}$) are calculated (not shown). However, no significant correlations are detected. Nonetheless, it is noticed that θ_{RF} and $|v|$ of the two return flows differ; most of the time, the right return flows are directed more downwards than the left return flows and have a higher velocity magnitude. Such imbalance may impact the merged jet movement, which—on average—is oriented slightly towards the left as mentioned earlier in Sect. 4.1. A further discussion on the potential influence of the return flows on the overall flow behaviour is provided in Sect. 4.4. The interested reader is referred to Thysen (2022) for additional results regarding the return flow characteristics.

4.3 Instantaneous flow: vortical structures

Vortices with a range of length scales are present throughout the flow field. Figure 9 presents an example of vortices that are formed in the outer layer of the (left) ceiling jet (for $Re_0 \approx 3450$ only), using instantaneous velocity vectors from which the area-averaged instantaneous velocity is subtracted, and with the vortex centres being visualised using $|\Gamma|$. These vortex trains are similar to those described in van Hooff et al. (2012), who addressed such vortices to be generated from Kelvin–Helmholtz instabilities. The Strouhal number ($St = fh/U_{J,0}$) based on the vortex formation frequency ($f \approx 18$–29 Hz), which is derived from the average distance between two adjacent vortices and $U_{J,0}$ (van Hooff et al. 2012), varies within the range $5.4 \times 10^{-1} < St < 6.3 \times 10^{-1}$ for the two jets and the different Re_0. It was not possible to use FFT to obtain f because of f_s being too low (15 Hz).

Vortical structures are also frequently observed along both sides of the merged jet for all Re_0 (see e.g. Figure 4a). Figure 10 illustrates using velocity vectors (only one out of two vectors is shown) and contours of $|\Gamma|$ for $Re_0 \approx 3450$ and 4350, that the vortices appear to be either those generated from below the inlet slots (Fig. 10a), or vortices "rolling up" from the coalescence of the detached return flow and the merged jet (Fig. 10b). The frequency of vortices moving along the merged jet is found to vary around 1.3–2.6 Hz ($3.9 \cdot 10^{-2} < St = fh/U_0 < 6.1 \cdot 10^{-2}$) for the three Re_0. It is verified that these vortices cause higher fluctuations in the recorded velocities when passing the corresponding monitoring point;

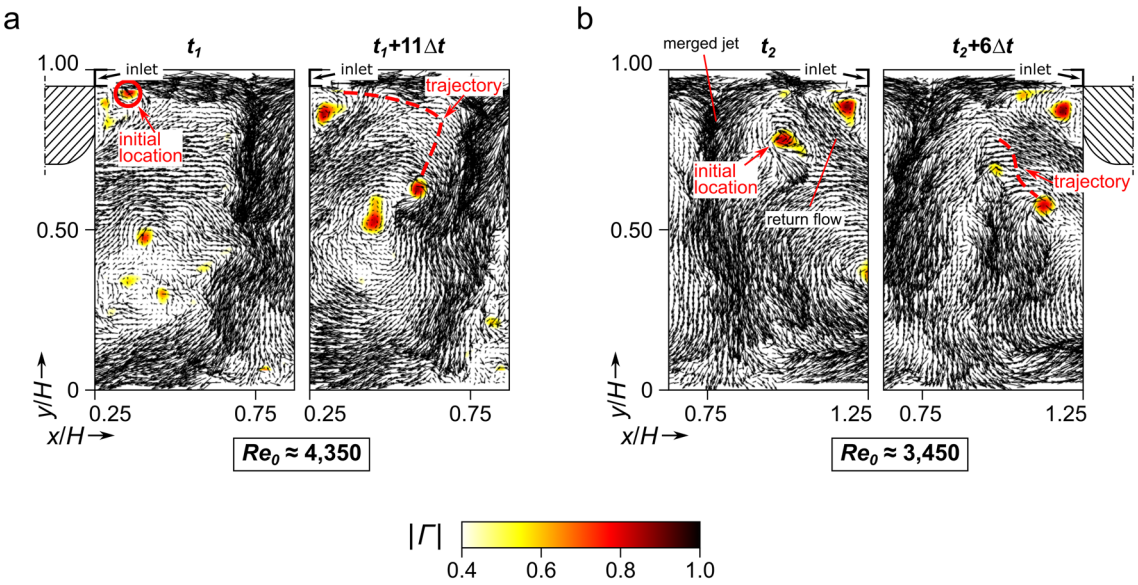

Fig. 10 Vortex generation and transport along opposing ceiling jets and merged jet, visualised using velocity vectors and contours of $|\Gamma|$: **a** vortices generated below inlets that are transported along both sides of merged jet, **b** vortices developed from coalescence of return flow and merged jet. Vortex trajectories are indicated by red dashed lines and $\Delta t = f_s^{-1}$. Note that vector fields are shown for $x/H > 0.25$ (edge left OHSC) or $x/H < 1.25$ (edge right OHSC), and hence vectors below OHSC are not presented

however, because of their non-continuous passage along the merged jet (due to e.g. vortex breakup) and, in addition, some of the vortices not being recorded since they did not pass the monitoring point (attributed to e.g. the transient horizontal movement of the merged jet), no peaks are observed in the energy spectra at these frequencies (Fig. 8). The number of vortices moving along the right side of the merged jet is also observed to be higher than at the left side for all Re_0.

These vortices can transport high-momentum fluid from within the merged jet towards the outer areas (Fig. 10), causing a strong widening of the merged jet. In particular during the instability events in $Re_0 \approx 3450$ (Fig. 6, Online Resources 2 and 3), the vortices can become very pronounced and split off from the outer layer of the ceiling jets while carrying high-momentum fluid throughout the enclosure (e.g. Figure 6 at $t_0 + 35\Delta t$; $x/H \approx 0.37$ and $y/H \approx 0.75$). Eventually, the vortices break up or merge with other vortices within the large recirculation cells.

The two large recirculation cells at both sides of the merged jet have centres which are moving throughout the enclosure as shown by the distribution plots of the centre locations in Fig. 11. From each PIV sample, the centre location is detected using $|\Gamma|$ and the relative frequency of each location is determined. For $Re_0 \approx 3450$, the recirculation centres are less concentrated (absence of red colours) and cover a slightly larger area, indicating a less stable recirculation centre compared to $Re_0 \approx 4350$ (and $Re_0 \approx 4650$). Due to the low velocities within these centres, such concentrated distributions may indicate poor mixing in these areas, in which contaminants could remain locked-up as in for example ventilation applications (e.g. van Hooff et al. 2013; Cao and Meyers 2013).

4.4 Discussion

From the above analyses of the instantaneous flow, better insights into the mean flow characteristics (Sect. 4.1) are obtained. As addressed in Thysen et al. (2022a), the left ceiling jet always has (slightly) higher momentum than the right one, resulting in $X_{c,IZ}/H > 0.75$. Kind and Suthanthiran (1973) and Gilbert (1985, 1989) described that the merged jet in an open environment was directed away from the supply jet with higher momentum, which would be to the right in the current study. Yet, the opposite is observed (Fig. 3), which shows the effect of the enclosed domain, inducing impingement of the merged jet on the floor (cf. Rockwell 1979) and an interaction with the return flows. In addition, it is hypothesised that, due the interaction zone being on average located closer to the right (suppressed) supply jet ($X_{c,IZ}/H > 0.75$), the turning effect at this side increases—which is the driver of the vortices together with the head-on collision (Gilbert 1985)—resulting in an imbalance in number of vortices generated at both inlets that will pass along the merged jet. This could explain the observed asymmetry in $X_{½m}$ (Sect. 4.1) and the higher momentum of the right return flow compared to the left one (Sect. 4.2). The inlet conditions and the confinement (enclosed domain) may thus

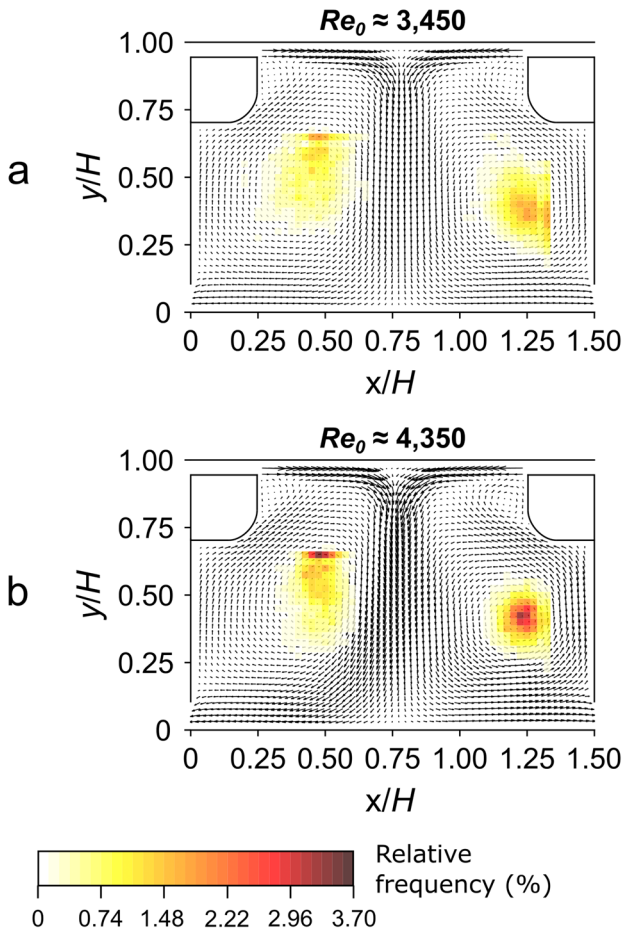

Fig. 11 Distribution of centre location of two large recirculation cells in ceiling-jet configuration plotted on top of mean velocity vector field (Fig. 3) for **a** $Re_0 \approx 3450$ and **b** $Re_0 \approx 4350$

have a large impact on the resulting flow field. However, it should be mentioned that the complex interaction between the different flow components makes a straightforward cause-and-effect analysis difficult. For example, the detached return flows can also influence the supply jets' momentum at the point of interaction, or they can affect the momentum of the small recirculation cells (VIII in Fig. 2a) that may influence shear stresses and hence vortex generation.

Thysen et al. (2022a) found similarities between the merged jet mean velocity and turbulence profiles with those of a turbulent plane free jet (generated from a single nozzle in an open domain). The growth rate of the merged jet, however, was up to 3.4 times larger, partly due to increased turbulence levels compared to the plane free jet. The current paper demonstrates that the passage of vortices and the horizontal flapping movement can contribute in this respect. The absence of a specific flapping frequency is different than reported for the free plane jet by Cervantes de Gortari and Goldschmidt (1981), who derived $St = fh/U_0$ to be in the range of 7×10^{-4} to 8×10^{-2}. Körner et al. (2013) investigated opposing wall jets in an (isothermal air-filled reduced-scale) generic model room (Sect. 1) and also observed the large-scale flow structures to oscillate at specific frequencies in the range of 0.16–1.37 Hz (from which $6.2 \times 10^{-4} < St = fh/U_0 < 7.6 \times 10^{-4}$ can be deduced). Gilbert (1985), who studied a merged jet arising from opposing wall jets in an open environment, did not observe jet flapping at all, based on their calculations of correlations (cf. Equation 1). It should be mentioned that many aspects can result in differences between this and former studies, such as the enclosed domain (flow impingement, return flows), the relatively short distance between the ceiling jets (d_{ci}) which are also transitional (i.e. not yet turbulent) at the point of interaction, absence of a self-similar turbulence intensity of the merged jet (Thysen et al. 2022a), etc. The comparison with the literature hence solely serves the purpose of obtaining additional insights into the presented results and to check for overall trends between comparable opposing-jet configurations.

5 PIV measurement results: lateral inlets

5.1 Mean flow

The measurements in the lateral-jet configuration (Fig. 2b) for the three different Re_0 all show very similar mean and instantaneous flow patterns, represented in Fig. 12 by mean velocity vectors of the measurement with $Re_0 \approx 4300$. Note that only one out of three vectors is depicted in Fig. 12a and one out of two in Fig. 12b–h for the sake of clarity. The mean flow field (Fig. 12a)—again obtained after averaging over all recorded PIV samples (15 min)—shows that the two lateral jets, which are initially wall jets but transition to free jets at $x/H = 0.125$ (left) and $x/H = 1.375$ (right), collide around the centreline of the enclosure ($x/H = 0.75$) and form a downward flowing merged jet with mean location $X_{c,MJ}/H$, indicated by the green dash-dotted line (see also Fig. 2b), equal to 0.80 ($Re_0 \approx 3500$), 0.79 ($Re_0 \approx 4300$) and 0.76 ($Re_0 \approx 4600$). Two large recirculation cells on each side of the merged jet are present and two smaller recirculation cells exist above the lateral jets (i.e. in between the two OHSCs), the centres of which are visualised using contours of $|\Gamma|$. More details on the average flow characteristics can be found in Thysen et al. (2022a).

5.2 Instantaneous flow: overall flow behaviour

The typical instantaneous flow patterns in Fig. 12b–h show the transient flow field, driven by the unstable interplay of the opposing jets. The corresponding flow animation is Online Resource 4 in the supplementary information section. The instance at which the two lateral jets impinge on each other (Fig. 12b) evolves towards a situation with

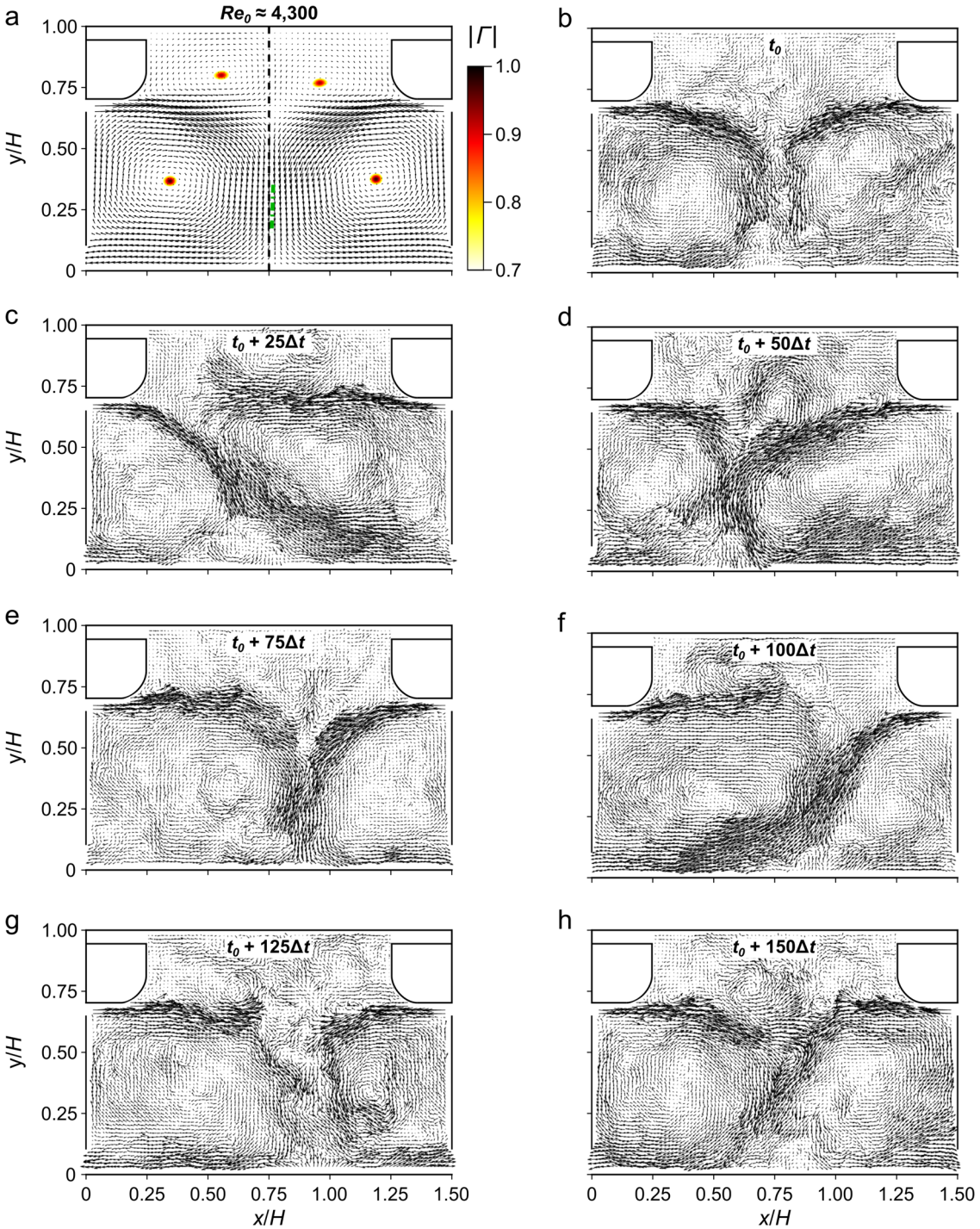

Fig. 12 Mean (**a**) and instantaneous (**b–h**) velocity vectors in vertical midplane of lateral-jet configuration for $Re_0 \approx 4300$ ($\Delta t = f_s^{-1}$). Green dash-dotted line in **a** indicates $X_{c,MJ}$ over height of merged jet. Corresponding animation is Online Resource 4

the jets deflecting in opposite directions, one jet directed downwards while the other is directed more towards the ceiling (Fig. 12c). Then, a transition takes place (Fig. 12d,e) to a similar but inverse state, i.e. the other jet is now directed downwards and flowing underneath the opposing jet (Fig. 12f), after which the initial situation is reached again (Fig. 12g,h). The alternation in jet deflections seems to be repeated most of the time, i.e. quasi-periodic deflecting oscillations are present.

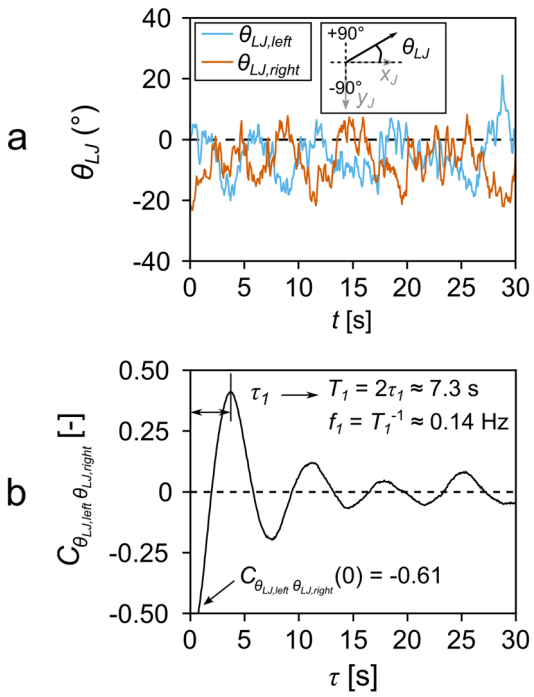

Fig. 13 Direction angles of opposing lateral jets (θ_{LJ}) after detachment from OHSCs for $Re_0 \approx 4300$: **a** first 30 s of time series; **b** corresponding CCF between θ_{LJ} of each jet

The deflecting oscillation of the left and right lateral jets also becomes apparent from tracking their direction angle with respect to the horizontal θ_{LJ} over time (after detachment from the OHSCs), as shown in Fig. 13a for the measurement with $Re_0 \approx 4300$. A negative angle indicates a downward directed jet. Both jets clearly show quasi-periodic oscillations, with one jet moving out of phase with respect to the other, as confirmed by their oscillating CCF in Fig. 13b with negative correlation coefficient (i.e. at $\tau = 0$). Note that the range of the correlation plot is adjusted for better visibility and that the correlation coefficient goes to −0.61. Following Cervantes de Gortari and Goldschmidt (1981), the period of the deflecting oscillation T_1 can be determined from the CCF as $2\tau_1 \approx 7.3$ s with τ_1 as indicated in Fig. 13b, corresponding to a frequency $f_1 \approx 0.14$ Hz. Similar periods are obtained in the two other measurements: 7.9 s (0.13 Hz) at $Re_0 \approx 3500$ and 7.0 s (0.14 Hz) at $Re_0 \approx 4600$. In addition, both lateral jets are observed to have similar distribution plots of θ_{LJ} over time (not shown).

A similar analysis is performed for the x-velocity fluctuations in three monitoring points (Fig. 2b), which are located right above the detached lateral jet (point A), in the interaction zone (point B) and in the merged jet (point C), presented for $Re_0 \approx 4300$ in Fig. 14a–c, respectively (the outcomes for the other two Re_0 are again very similar and therefore not shown). The top images show fragments of the time series of the dimensionless x-velocity (u/U_0), which clearly exhibit oscillatory behaviour. This is also observed in the ACFs shown in the middle images. Note that the range of the correlation plots is restricted for better visibility (C_{uu} goes to 1 at $\tau = 0$). Two particular periods can be directly derived from the ACFs, i.e. $T_1 \approx 7.1$–7.3 s (Fig. 14a, b) and $T_2 \approx 2.6$ s (Fig. 14c), based on $2\tau_1$ and $2\tau_2$, corresponding to frequencies $f_1 \approx 0.14$ Hz and $f_2 \approx 0.38$ Hz, respectively. The corresponding Strouhal numbers $St = fh/U_0$ are $St_1 \approx 3.3 \cdot 10^{-3}$ and $St_2 \approx 8.9 \cdot 10^{-3}$. The 1D energy spectra presented in the bottom images confirm the presence of two dominant frequencies in most of the monitoring points: a group with relatively high energy levels centred around St_1 and a second group of smaller peaks around St_2. The lower frequency (f_1) is in agreement with the frequency determined earlier for θ_{LJ} (deflecting oscillations). The higher frequency (f_2), mainly detected in points B and C, may be attributed to the additional (smaller-scale) transient horizontal movement of the interaction zone and merged jet related to the interaction (impingement) between the jets, presented in Online Resource 5.

5.3 Instantaneous flow: vortical structures

At both sides of the lateral jets vortices are generated due to shear instabilities resulting in asymmetric vortex trains, as shown in Fig. 15 for $Re_0 \approx 4300$ by instantaneous velocity vectors from which the area-averaged velocity is subtracted, together with contours of $|\Gamma|$ to visualise the vortex centres. The vortices seem to be continuously formed with formation frequency $f \approx 16$–23 Hz (all Re_0), based on the average distance between two adjacent vortices and $U_{J,0}$. The corresponding Strouhal number is $4.8 \cdot 10^{-1} < St = fh/U_{J,0} < 5.2 \cdot 10^{-1}$. Additional vortices develop from shear effects induced by the jet interaction. Tracking of the vortices over time (not shown) demonstrates that they can merge with other vortices, grow relatively large or break up. The large vortices, when present, are observed to develop above the dominant (upper) jet. The interested reader is referred to Thysen (2022) for more detailed information.

The area below the lateral inlets is dominated by the two large recirculation cells. Figure 16 visualises their centre location recorded in every PIV sample and indicates the relative frequency of each location. Both recirculation cells show a similar distribution, with the centre of the cells only covering a restricted area of the enclosure. Together with the centres being characterised by relatively low velocities, this could lead to lock-up of contaminants, similar as mentioned in studies on airplane cabin ventilation with opposing lateral jets (e.g. Li et al. 2015, 2017). As shown in Fig. 12, the merged jet is always maintained during the deflecting oscillations, which makes the recirculation centres rather shielded from fresh supply fluid as the lateral jets do not flow across the centres.

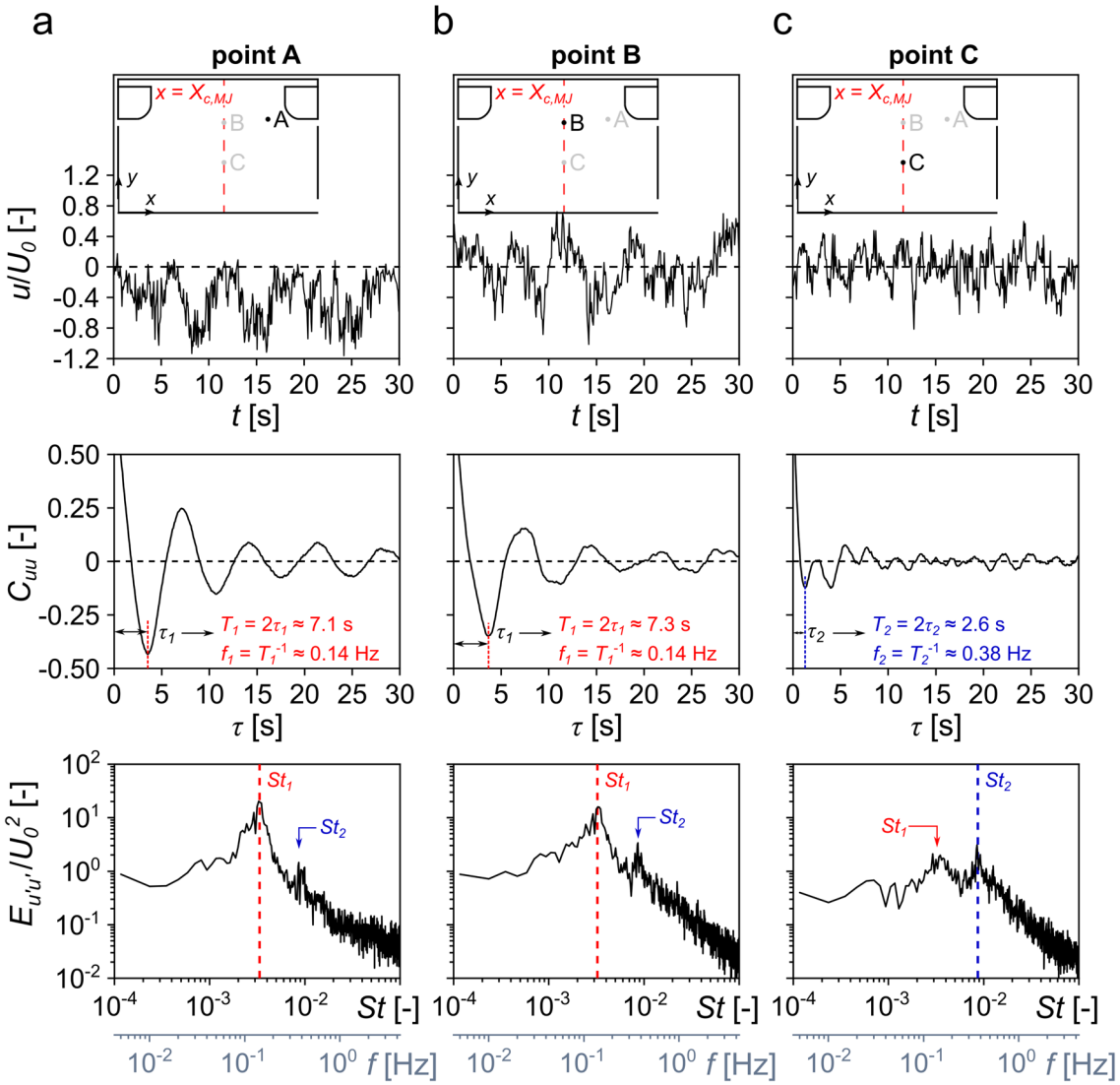

Fig. 14 Fragment (first 30 s) of time series of dimensionless x-velocity (top) with corresponding ACF (middle) and 1D energy spectrum (bottom) in monitoring points (see also Fig. 2b) in lateral-jet configuration for $Re_0 \approx 4300$: **a** point A, **b** point B and **c** point C

5.4 Discussion

The deflecting oscillation of the lateral jets presented above shows similarities with the aforementioned literature on opposing plane free jets (Sect. 1). According to the maps of parameter space reported in Denshchikov et al. (1978, 1983), Li et al. (2011) and Tu et al. (2014), deflecting oscillations are to be expected with values of the parameters Re_0 and AR as in the current measurements. Recalculation of the Strouhal number in terms of the jet-separation distance d (instead of h), as frequently reported in the literature, yields $St_d = fd/U_0 \approx 9.8 \cdot 10^{-2}$. Denshchikov et al. (1978, 1983) reported periods between 2 and 30 s in their experiments with opposing plane water jets for a variety of Re_0 and AR values, following the empirically derived relation $T \approx 6d/U_0$, from which $St_d \approx 1.7 \cdot 10^{-1}$ can be deduced. Li et al. (2011) reported $1.0 \cdot 10^{-1} < St_d < 2.0 \cdot 10^{-1}$ and Hassaballa and Ziada (2015) found $1.0 \cdot 10^{-1} < St_d < 1.6 \cdot 10^{-1}$ for the deflecting oscillations between opposing plane air jets. However, note that these studies are all performed in a non-enclosed environment and that the oscillation frequency tends to decrease with the level of confinement (Li et al. 2013; Tu et al. 2014), which would result in lower St_d (with d/U_0 fixed), and would thus be more in agreement with $St_d \approx 9.8 \cdot 10^{-2}$ observed in the current paper. In addition, the set-up in the current paper includes OHSCs, which may also affect the lateral jet movement due to jet detachment (Coanda effect) at the rounded part of the OHSCs. The deflections are self-sustained, initiated by the unstable head-on collision of the opposing jets and driven by a pressure

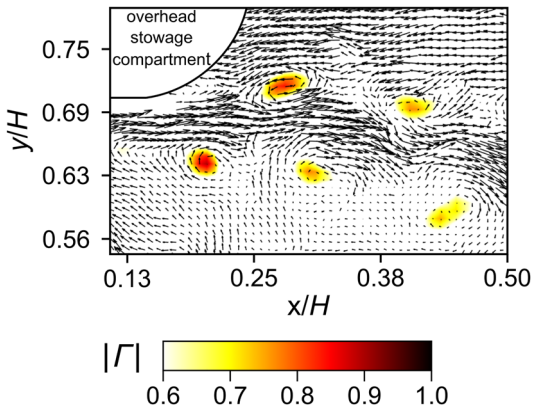

Fig. 15 Vortex trains at both sides of (left) lateral jet ($Re_0 \approx 4300$), visualised by vectors of instantaneous velocity from which area-averaged instantaneous velocity is subtracted and contours of $|\Gamma|$

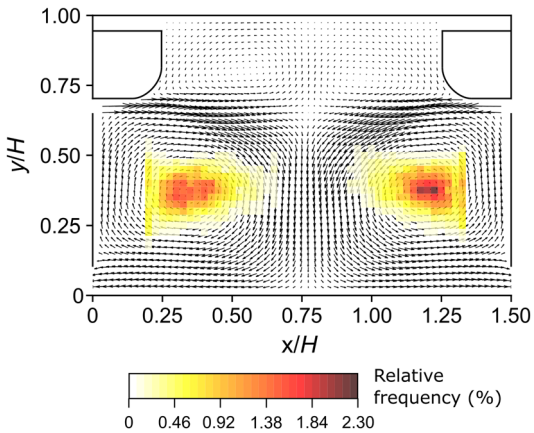

Fig. 16 Distribution of centre location of two large recirculation cells in lateral-jet configuration plotted on top of mean velocity vector field (Fig. 12a) for $Re_0 \approx 4300$

release and feedback mechanism as described by Li et al. (2013) and Tu et al. (2014).

The deflecting movements observed in the current study also resemble the large-scale swing motions that may occur in airplane cabin opposing-jet mixing ventilation flows with lateral jets (e.g. Yang et al. 2016; Li et al. 2016, 2017; Wang et al. 2022). The airplane cabin environment contains many complex factors that affect the oscillation period of the swing movements, such as the specific cabin geometry, obstacles (seats, passengers), inlet conditions (velocity and direction angle), thermal conditions, etc. Reported periods in cabin mock-ups under isothermal conditions range from 3.3–10 s (Wang et al. 2022) to 25.2–29.8 s (Li et al. 2017), from which it is obtained that $St_d \approx 0.21$–0.31 and 0.05–0.06, respectively. Under non-isothermal (cooling) conditions, the swing motions are more restrained, which could either lead to longer periods (26.7–45.1 s, $St_d \approx 0.04$–0.07) reported by Wang et al. (2021) or, on the contrary, to less periodicity and shorter periods (13–19.8 s, $St_d \approx 0.05$–0.06) according to Li et al. (2017). Li et al. (2016) showed that horizontal oscillations with both jets displacing one another but flowing downwards could occur when cooling (i.e. very small amplitude of the deflecting oscillations). This was also reported by Wang et al. (2021) for small U_0 and under isothermal conditions. It should be mentioned that the purpose of the current study is not to replicate the flow inside a real airplane cabin, rather the generic set-up is created to incorporate the important flow phenomena and fundamental flow components that are inherent to, among other things, airplane cabin mixing ventilation flows, which is demonstrated by e.g. the presence of deflecting jet oscillations.

6 Limitations and future work

Although it was possible to visualise vortices using velocity vectors and Γ (from the vortex centre identification algorithm), a higher sampling frequency (> 15 Hz) or spatial resolution (< 1.54 mm) may be desired for improved vortex identification and tracking of the transported vortices, which could be realised in future measurements by high-frequency PIV or by focusing on specific parts of the flow field, respectively. This will allow to further investigate the influence of vortices on the transient jet interaction, which, for example in the lateral-jet configuration, may be involved in the driving mechanism of the deflecting oscillations (Hassaballa and Ziada 2015). In addition, future measurements may use laser Doppler anemometry (LDA) to obtain detailed spectral information, or fluorescent dye for flow visualisations (similar as in van Hooff et al. 2012).

It is carefully checked and confirmed that the inlet velocities remained statistically steady during the course of the measurements and that no sudden increase of the inlet velocity fluctuations occurred. Also the inlet velocities appear not to have any characteristic frequency (at least, in the measured frequency range $< f_s/2$), which are factors that could have initiated the larger range of $X_{c,MJ}/H$ or the persistent deviating flow patterns (apparent flow instabilities) in the ceiling-jet configuration with $Re_0 \approx 3450$. Additional measurements may consider other vertical and horizontal measurement planes for inspection of the flow in the whole enclosure, since 3D flow structures may also play a role in this regard.

The reduced-scale experimental set-up is designed to study opposing-jet flows, such as encountered in airplane cabin mixing ventilation. It is clear that the enclosure is simplified and differs from e.g. the complex geometry of a real airplane cabin in which e.g. seats, passengers and heat sources, or the particular supply configuration (using lateral and/or ceiling slots), unequivocally affect the overall flow

field. However, as shown in this paper, the current set-up is able to provide the fundamental flow components/phenomena representative of cabin mixing ventilation (e.g. deflecting oscillations, lock-up phenomena, etc.). Due to the generic character of the enclosure, a detailed flow analysis can be performed that is useful to (and has not yet been performed in) airplane cabins and other opposing-jet applications (Sect. 1). Nevertheless, future work could focus on the inclusion of (heated) obstacles or on configurations with a simultaneous flow from both the lateral and ceiling inlets. Additional measurements with reduced supply flow rates in the lateral-jet configuration may also be valuable in order to examine the threshold supply-jet velocity needed to still provoke deflecting oscillations. This is motivated by previous studies (mentioned in Sects. 1 and 5.4) that showed restrained deflecting oscillations for small inlet velocities, which could have a strong impact on, for example, the dilution of airborne contaminants (and hence the ventilation efficiency). Other future work may consist of measurements in the configuration without OHSCs, which may serve as a model of an empty room, for example useful for building ventilation flows.

Another advantage of using a generic enclosure is the ease of implementation in CFD simulations. The geometry, inlet and boundary conditions can be accurately reproduced, as already illustrated in a previous numerical study by the authors (Thysen et al. 2021). In this study, the measurement data served as benchmark for (sub-configuration) validation of CFD simulations, confirming that the transient nature of the jet interaction and the generation of vortices observed in the current paper, require transient approaches—such as large eddy simulation (LES)—to correctly model the opposing-jet flow. Also, since the opposing jets produce instantaneous flow patterns that are asymmetric with respect to the vertical cross-section of the enclosure ($x/H = 0.75$)—though the eventual mean flow field can be close to symmetric, application of a symmetry condition at the cross-section as often used in CFD studies on airplane ventilation (e.g. Pang et al. 2018; Yan et al. 2020) and other applications (e.g. Wood et al. 1991), may be improper to model the real flow field. Future work should continue sub-configuration validation with as aim to eventually perform CFD simulations in realistic airplane cabins to improve the efficiency of conventional mixing ventilation, as for example illustrated in Thysen et al. (2022b).

7 Conclusions

This paper presents analyses of the instantaneous behaviour of two isothermal interacting opposing plane jets measured with 2D PIV in a reduced-scale water-filled generic enclosure. Both wall jets (ceiling jets) and free jets (lateral jets) are examined, with inlet Reynolds numbers in the (transitional) range of 3450–4650. Such opposing jets are, for example, the driving force of mixing ventilation in (airplane) cabins.

The following main conclusions are obtained for the configuration with opposing plane wall jets:

- The jet interaction is transient, resulting in an alternating horizontal movement of the interaction zone. The merged jet resembles the flapping of a turbulent plane jet and its location is correlated to this of the interaction zone.
- The 1D energy spectra (FFT) do not reveal a particular frequency of the jet flapping.
- Vortices develop from the shear layers below the inlets (vortex trains; $5.4 \times 10^{-1} < \mathrm{St} = fh/U_{J,0} < 6.3 \times 10^{-1}$) and/or at both sides along the merged jet (interaction with return flow; $3.9 \times 10^{-2} < \mathrm{St} = fh/U_0 < 6.1 \times 10^{-2}$). They can contribute significantly to the mixing of high-momentum fluid within the merged jet and surrounding fluid, with a distinct effect on the mean flow patterns.
- The centres of the two large recirculation cells are rather stable (limited spatial extent) and stagnant (low velocity), which may indicate poor mixing in these areas.

The following main conclusions can be drawn for the configuration with opposing plane free jets:

- The jet interaction is unstable and characterised by quasi-periodic deflecting oscillations, superposed onto the transient horizontal movement of the interaction zone and merged jet (jets impinging on each other and displacing each other).
- The jet deflections occur at frequency 0.13–0.14 Hz or $\mathrm{St} = fh/U_0 \approx 3.3 \cdot 10^{-3}$. The frequency presumably related to the transient movement amounts 0.38 Hz ($\mathrm{St} \approx 8.9 \cdot 10^{-3}$), but is much less energetic (FFT) than this of the deflecting oscillations.
- The jet deflections show similarities with the deflecting oscillations observed in the literature for opposing plane free jets in an open environment or for interacting lateral jets in an airplane cabin.
- Asymmetric vortex trains are formed at both sides of the free jets ($4.8 \cdot 10^{-1} < \mathrm{St} = fh/U_{J,0} < 5.2 \cdot 10^{-1}$) and multiple vortices can develop from the jet interaction, which can grow to a considerable size (e.g. above the dominant jet).
- The centres of the two large recirculation cells show to be shielded from the supply flow (low-velocity zones) and are rather stable (covering a limited area), which can result in contaminant lock-up.

Supplementary Information The online version contains supplementary material available at https://doi.org/10.1007/s00348-022-03549-9.

Acknowledgements The Research Foundation—Flanders (FWO), is gratefully acknowledged for their financial support of the PhD fellowship of Jo-Hendrik Thysen (project FWO 1150617N) and the funding for the development of the experimental set-up (FWO 1518517N). The authors are grateful to Airbus for supporting the measurement campaign. Special thanks go to Jan Diepens, Geert-Jan Maas and Stan van Asten, members of the Laboratory of the Unit Building Physics and Services at Eindhoven University of Technology, and Ad Holten, member of the Laboratory of the Fluids and Flows (F&F) section at Eindhoven University of Technology, for their valuable contributions.

Funding Fonds Wetenschappelijk Onderzoek, FWO 1150617 N, Jo-Hendrik Thysen, FWO 1518517 N.

Declarations

Conflict of interest The authors have no conflict of interest to declare.

References

Ansari A, Chen KK, Burrell RR, Egolfopoulos FN (2018) Effects of confinement, geometry, inlet velocity profile, and Reynolds number on the asymmetry of opposed-jet flows. Theor Comp Fluid Dyn 32:349–369. https://doi.org/10.1007/s00162-018-0457-1

ASHRAE handbook: heating, ventilating and air-conditioning applications, Inch-Pound Edition (2019) American Society of heating, refrigerating and air-conditioning engineers (ASHRAE), Atlanta, GA

Besbes S, Mhiri H, Palec GL, Bournot P (2003) Numerical and experimental study of two turbulent opposed plane jets. Heat Mass Transfer 39:675–686. https://doi.org/10.1007/s00231-002-0336-5

Cao SJ, Meyers J (2013) Influence of turbulent boundary conditions on RANS simulations of pollutant dispersion in mechanically ventilated enclosures with transitional slot Reynolds number. Build Environ 59:397–407. https://doi.org/10.1016/j.buildenv.2012.09.004

Cao X, Liu J, Pei J, Zhang Y, Li J, Zhu X (2014) 2D-PIV measurement of aircraft cabin air distribution with a high spatial resolution. Build Environ 82:9–19. https://doi.org/10.1016/j.buildenv.2014.07.027

Cervantes de Gortari J, Goldschmidt VW (1981) The apparent flapping motion of a turbulent plane jet – further experimental results. J Fluid Eng T ASME 103:119–126. https://doi.org/10.1115/1.3240757

Champion M, Libby PA (1993) Reynolds stress description of opposed and impinging turbulent jets. Part I: closely spaced opposed jets. Phys Fluids A Fluid 5:203–216. https://doi.org/10.1063/1.858776

Denshchikov VA, Kondrat'ev VN, Romashov AN (1978) Interaction between two opposed jets. Fluid Dyn 13:924–926. https://doi.org/10.1007/BF01050971

Denshchikov VA, Kondrat'ev VN, Romashov AN, Chubarov VM (1983) Auto-oscillations of planar colliding jets. Fluid Dyn 18:460–462. https://doi.org/10.1007/BF01090570

Gilbert BL (1985) An investigation of turbulence mechanisms in V/STOL upwash flow fields, Grumman R&D Center Report RE-707

Gilbert B (1989) Turbulence measurements in a flow generated by the collision of radially flowing wall jets. Exp Fluids 7:103–110. https://doi.org/10.1007/BF00207302

Graftieaux L, Michard M, Grosjean N (2001) Combining PIV, POD and vortex identification algorithms for the study of unsteady turbulent swirling flows. Meas Sci Technol 12:1422–1429. https://doi.org/10.1088/0957-0233/12/9/307

Hassaballa M, Ziada S (2015) Self-excited oscillations of two opposing planar air jets. Phys Fluids 27:014109. https://doi.org/10.1063/1.4906235

Hunt HE, Space DR (1994) The airplane cabin environment: issues pertaining to flight attendant comfort

Johansson PS, Andersson HI (2005) Direct numerical simulation of two opposing wall jets. Phys Fluids 17:055109. https://doi.org/10.1063/1.1920627

Kandzia C, Mueller D (2016) Flow structures and Reynolds number effects in a simplified ventilated room experiment. Int J Vent 15:31–44. https://doi.org/10.1080/14733315.2016.1173291

Kandzia C, Mueller D (2018) Stability of large room airflow structures in a ventilated room. Int J Vent 17:2–16. https://doi.org/10.1080/14733315.2017.1332730

Keane RD, Adrian RJ (1990) Optimization of particle image velocimeters. Part I: double pulsed systems. Meas Sci Technol 1:1202–1215. https://doi.org/10.1088/0957-0233/1/11/013

Khayrullina A, van Hooff T, Blocken B, van Heijst GJF (2017) PIV measurements of isothermal plane turbulent impinging jets at moderate Reynolds numbers. Exp Fluids 58:31. https://doi.org/10.1007/s00348-017-2315-0

Kind RJ, Suthanthiran K (1973) The interaction of two opposing plane turbulent wall jets. J Fluid Mech 58:389–402. https://doi.org/10.1017/S002211207300265X

Körner M, Resagk C, Thess A (2015) Rayleigh number dependence of the Archimedes number dependent large-scale flow structure formation in mixed convection. In: 15th European turbulence conference, Delft, The Netherlands

Körner M, Shishkina O, Wagner C, Thess A (2013) Properties of large-scale flow structures in an isothermal ventilated room. Build Environ 59:563–574. https://doi.org/10.1016/j.buildenv.2012.10.011

Kotansky DR, Glaze LW (1980) The effects of ground wall-jet characteristics on fountain upwash flow formation and development. Report ONR-CR212-261-1F

Kühn M, Bosbach J, Wagner C (2009) Experimental parametric study of forced and mixed convection in a passenger aircraft cabin mock-up. Build Environ 44:961–970. https://doi.org/10.1016/j.buildenv.2008.06.020

Li WF, Yao TL, Liu HF, Wang FC (2011) Experimental investigation of flow regimes of axisymmetric and planar opposed jets. AIChE J 57:1434–1445. https://doi.org/10.1002/aic.12369

Li WF, Huang GF, Tu GY, Liu HF, Wang FC (2013) Experimental study of planar opposed jets with acoustic excitation. Phys Fluids 25:014108. https://doi.org/10.1063/1.4788933

Li M, Zhao B, Tu J, Yan Y (2015) Study on the carbon dioxide lockup phenomenon in aircraft cabin by computational fluid dynamics. Build Simul 8:431–441. https://doi.org/10.1007/s12273-015-0217-8

Li J, Liu J, Cao X, Jiang N (2016) Experimental study of transient air distribution of a jet collision region in an aircraft cabin mock-up. Energ Build 127:786–793. https://doi.org/10.1016/j.enbuild.2016.06.039

Li J, Liu J, Wang C, Wesseling M, Müller D (2017) PIV experimental study of the large-scale dynamic airflow structures in an aircraft cabin: swing and oscillation. Build Environ 125:180–191. https://doi.org/10.1016/j.buildenv.2017.07.043

Lin CH, Horstman RH, Ahlers MF, Sedgwick LM, Dunn KH, Topmiller JL, Bennett JS, Wirogo S (2005) Numerical simulation of airflow and airborne pathogen transport in aircraft cabins–part i: numerical simulation of the flow field. ASHRAE Tran 111:755–763

Liu Y, Fox RO (2006) CFD predictions for chemical processing in a confined impinging-jets reactor. Aiche J 52:731–744. https://doi.org/10.1002/aic.10633

Liu D, Zhao FY, Tang GF (2010) Non-unique convection in a three-dimensional slot-vented cavity with opposed jets. Int J Heat Mass

Tran 53:1044–1056. https://doi.org/10.1016/j.ijheatmasstransfer.2009.11.006
Pang L, Li P, Bai L, Liu D, Zhou Y, Yao J (2018) Optimization of air distribution mode coupled interior design for civil aircraft cabin. Build Environ 134:131–145. https://doi.org/10.1016/j.buildenv.2018.02.019
Pawlowski RP, Salinger AG, Shadid JN, Mountziaris TJ (2006) Bifurcation and stability analysis of laminar isothermal counterflowing jets. J Fluid Mech 551:117–139. https://doi.org/10.1017/S0022112005008396
Prasad AK (2000) Particle image velocimetry. Curr Sci 79:51–60
Puech T, Boussard M, D'amato A, Millerand G (2020) A fully automated periodicity detection in time series. In: Lemaire V, Malinowski S, Bagnall A, Bondu A, Guyet T, Tavenard R (eds) Advanced analytics and learning on temporal data. AALTD 2019. Lecture Notes in Computer Science, vol 11986. Springer, Cham. https://doi.org/10.1007/978-3-030-39098-3_4
Raffel M, Willert CE, Scarano F, Kähler CJ, Wereley ST, Kompenhans J (2018) Particle Image Velocimetry: A Practical Guide. Springer, Berlin. https://doi.org/10.1007/978-3-319-68852-7
Rockwell D (1979) Self-sustained oscillations of impinging free shear layers. Ann Rev Fluid Mech 11:67–94. https://doi.org/10.1146/annurev.fl.11.010179.000435
Rolon JC, Veynante D, Martin JP (1991) Counter jet stagnation flows. Exp Fluids 11:313–324. https://doi.org/10.1007/BF00194863
Samaniego JM, Yip B, Poinsot T, Candel S (1993) Low-frequency combustion instability mechanisms in a side-dump combustor. Combust Flame 94:363–380. https://doi.org/10.1016/0010-2180(93)90120-R
Shishkina O, Wagner C (2012) A numerical study of turbulent mixed convection in an enclosure with heated rectangular elements. J Turbul 13:1–21. https://doi.org/10.1080/14685248.2012.677541
Stoica P, Moses RL (2005) Spectral analysis of signals. Upper Saddle River, New Jersey
Thatcher TL, Wilson DJ, Wood EE, Craig MJ, Sextro RG (2004) Pollutant dispersion in a large indoor space: part 1–scaled experiments using a water-filled model with occupants and furniture. Indoor Air 14:258–271
Thysen J-H (2022) Experimental and numerical analysis of isothermal opposing-jet flows: towards improved airplane cabin mixing ventilation efficiency. Dissertation, KU Leuven
Thysen J-H, van Hooff T, Blocken B, van Heijst GJF (2021) CFD simulations of two opposing plane wall jets in a generic empty airplane cabin: comparison of RANS and LES. Build Environ 205:108174. https://doi.org/10.1016/j.buildenv.2021.108174
Thysen J-H, van Hooff T, Blocken B, van Heijst GJF (2022a) PIV measurements of opposing-jet ventilation flow in a reduced-scale simplified empty airplane cabin. Eur J Mech B Fluid 94:212–227. https://doi.org/10.1016/j.euromechflu.2022.03.001
Thysen J-H, van Hooff T, Blocken B, van Heijst GJF (2022b) Airplane cabin mixing ventilation with time-periodic supply: Contaminant mass fluxes and ventilation efficiency. Indoor Air 32(11). https://doi.org/10.1111/ina.13151
Tu G, Li W, Du K, Huang G, Wang F (2014) Onset and influencing factors of deflecting oscillation in planar opposed jets. Chem Eng J 247:125–133. https://doi.org/10.1016/j.cej.2014.02.097
van Hooff T, Blocken B, Defraeye T, Carmeliet J, van Heijst GJF (2012) PIV measurements of a plane wall jet in a confined space at transitional slot Reynolds numbers. Exp Fluids 53:499–517. https://doi.org/10.1007/s00348-012-1305-5
van Hooff T, Blocken B, van Heijst GJF (2013) On the suitability of steady RANS CFD for forced mixing ventilation at transitional slot Reynolds numbers. Indoor Air 23:236–249. https://doi.org/10.1111/ina.12010
Vlachos M, Yu P, Castelli V (2005) On periodicity detection and structural periodic similarity. In: Proceedings of the 2005 SIAM international conference on data mining (SDM). https://doi.org/10.1137/1.9781611972757.40
Wang C, Liu J, Li J, Guo Y, Jiang N (2017) Turbulence characterization of instantaneous airflow in an aisle of an aircraft cabin mockup. Build Environ 116:207–217. https://doi.org/10.1016/j.buildenv.2017.02.015
Wang C, Zhang J, Chao J, Yang C, Chen H (2022) Evaluation of dynamic airflow structures in a single-aisle aircraft cabin mockup based on numerical simulation. Indoor Built Environ 31(2):398–413. https://doi.org/10.1177/1420326X21992094
Wood P, Hrymak A, Yeo R, Johnson D, Tyagi A (1991) Experimental and computational studies of the fluid mechanics in an opposed jet mixing head. Phys Fluids A-Fluid 3:1362–1368. https://doi.org/10.1063/1.858205
Yan Y, Li X, Yang L, Yan P, Tu J (2020) Evaluation of cough-jet effects on the transport characteristics of respiratory-induced contaminants in airline passengers' local environment. Build Environ 183:107206. https://doi.org/10.1016/j.buildenv.2020.107206
Yang C, Zhang X, Yao Z, Cao X, Liu J, He F (2016) Numerical study of the instantaneous flow fields by large eddy simulation and stability analysis in a single aisle cabin model. Build Environ 96:1–11. https://doi.org/10.1016/j.buildenv.2015.10.022
Zhao Y, Brodkey R (1998) Averaged and time-resolved, full-field (three-dimensional), measurements of unsteady opposed jets. Can J Chem Eng 76:536–545. https://doi.org/10.1002/cjce.5450760326
Zhao FY, Liu D, Tang GF (2008) Multiple steady fluid flows in a slot-ventilated enclosure. Int J Heat Fluid Fl 29:1295–1308. https://doi.org/10.1016/j.ijheatfluidflow.2008.06.005
Zigunov F (2021) 2D Vortex core tracking—gamma 1—super FAST. MATLAB Central File Exchange. https://www.mathworks.com/matlabcentral/fileexchange/72092-2d-vortex-core-tracking-gamma-1-super-fast. Accessed 20 Apr 2021